A geometrically nonlinear reduced-order method using hybrid-stress solid-shell formulations for 3D large deformation analysis of thin-walled structures

Liang, Ke; Mu, Jiaqi; Castro, Saullo G.P.

Important note
To cite this publication, please use the final published version (if applicable).
Please check the document version above.

A geometrically nonlinear reduced-order method using hybrid-stress solid-shell formulations for 3D large deformation analysis of thin-walled structures

Ke Liang [a,b],*, Jiaqi Mu [a], Saullo G.P. Castro [c],**

[a] *School of Aeronautics, Northwestern Polytechnical University, Xi'an 710072, PR China*
[b] *National Key Laboratory of Aircraft Configuration Design, Xi'an 710072, PR China*
[c] *Aerospace Structures & Materials, Delft University of Technology, Kluyverweg 1, 2629HS Delft, The Netherlands*

ARTICLE INFO

ABSTRACT

Post-buckling of thin-walled aeronautical structures induces failure modes related to skin-stiffener separation that require three-dimensional large deformation analyses for an accurate numerical prediction. Conventional finite elements are capable of solving such analyses, but with high associated computational costs, being therefore more utilized for the simulation of smaller structural components, or even restricted to perform virtual testing at coupon-level models. In this paper, a geometrically nonlinear reduced-order method using a hybrid-stress solid-shell formulation is proposed for large deformation analysis of thin-walled structures. Current reduced-order methods are mainly applicable to buckling problems, considering only the out-of-plane deformation. Furthermore, existing displacement-based reduced models involve a computationally expensive fourth-order tensor obtained with the higher-order strain energy variations. Here, a reduced-order model with only one degree of freedom is constructed for both in-plane and out-of-plane large deformation problems. It is shown that, with the hybrid-stress formulation, the constructional efficiency of the reduced system is largely improved by zeroing the fourth-order strain energy variation using the two-field Hellinger–Reissner variational principle, followed by a condensation of the stress terms that lead to a third-order approximation of the equilibrium equation. The nonlinear predictor solved by the reduced-order model can be corrected when its numerical accuracy is not satisfactory during the path-following analysis. A simple plate, a honeycomb cell with negative Poisson ratio, and a swept-back wing structure; are used as numerical examples to verify that the proposed method enables a superior path-following capability for the three-dimensional analysis of thin-walled structures undergoing large deflection, large rotation and large strains. Furthermore, an experimental validation of the proposed method is presented using a variable-thickness plate with mixed composite-metallic materials, undergoing large out-of-plane deflection.

1. Introduction

In the aeronautical and aerospace industries, thin-walled structures are extensively employed to efficiently withstand various external loads, significantly enhancing load-carrying capabilities without increasing structural weight. However, due to stringent lightweight design requirements, these structures often exhibit pronounced in-plane and out-of-plane deformations resulting from their inherently limited structural stiffness. Consequently, geometrically nonlinear analyses accounting for fully nonlinear kinematics are crucial for accurately capturing the complex three-dimensional (3D) large-deformation behavior of these structures.

Hybrid-stress FE formulations using a two-field (displacement and stress) variational principle have been applied to solid-shell elements. Sze et al. (2002) developed an eight-node hybrid-stress solid-shell element for the geometric nonlinear analysis of elastic shells based on the Hellinger–Reissner (HR) variational principle. Several studies have demonstrated that using the mixed stress–displacement formulation is more numerically robust when compared with the conventional displacement-based method, also enabling larger step sizes in the nonlinear path-following analysis (Magisano et al., 2017; Liguori and Madeo, 2021). However, incremental-iterative solutions of nonlinear equilibrium equations with multiple degrees-of-freedom require a high number of path-following steps to obtain the nonlinear response curve.

Various reduced-order methods have been developed to significantly decrease the number of degrees of freedom (DOFs) in the full-order nonlinear model of the conventional finite element method. According to whether the structural buckling is involved, the reduced-order methods are divided into two main categories. The first category refers to the methods for large deflection and rotation analysis without any buckling phenomena, for example the nonlinear reduced-order models developed by Wang et al. (2013), through extending the linearized modal models to the geometrically nonlinear analysis of cantilevered structures with large displacements/rotations. The curvatures can always be linearized using sufficient discretization, hence Drachinsky and Raveh (2020) proposed a modal-based method by constructing a reduced model using curvature modes for large deformation analysis of slender structures. A non-intrusive geometrically nonlinear augmentation method was developed by Cea and Palacios (2020) and Cea and Palacios (2022) using a two-step reduction technique and a mode-based Galerkin projection of intrinsic nonlinear equations. It should be noted that these reduced-order methods have the limitations of moderately large deflections (up to 50% span) and were not investigated for in-plane large deformation problems.

Another category of the reduced-order methods has been developed based on the Koiter's asymptotic theory (Koiter, 1967) to decrease the computational scale of nonlinear equilibrium equations required for buckling analysis (Barbero et al., 2014; Lanzo et al., 1995; Salerno and Lanzo, 1997; Henrichsen et al., 2016). Geometrical nonlinearities are normally accompanied by the structural buckling behavior (Kazinakis et al., 2021; Zhang and Kyriakides, 2024), including not only the post-buckling but also the pre-buckling regimes. The classical Koiter perturbation method constructed the reduced-order model only once at the bifurcation point, and were only applicable to the linear pre-buckling hypothesis and initial post-buckling analysis (Tiso, 2006). Garcea et al. (2009) and Zagari (2009) enlarged the range of validity of the reduced-order solution utilizing the asymptotic expansion based on the path tangent, buckling modes, and second-order modes of the structure. Liang et al. (2013, 2014) proposed a Koiter–Newton method to construct the reduced-order model at any point along the equilibrium path, and traced the geometrically nonlinear response of the structure in the presence of buckling. Although these reduced-order models significantly decrease the computational cost of the nonlinear buckling analysis, the Koiter's asymptotic theory requires the elemental strain energy variations up to the fourth-order with respect to the degrees of freedom, that is two orders higher than the conventional finite element method. In addition, the vast majority of the Koiter-based reduced-order methods is currently only applicable for buckling problems.

The main factor influencing the computational efficiency of the reduced-order method is the choice of nonlinear kinematics used for the calculation of high-order strain energy variations. The full Green–Lagrange nonlinear kinematics improve the range of validity of the reduced-order model for large deformation analysis, however the high-order strain energy variations create multiple dependencies between the translational and rotational degrees-of-freedom, and terms depending on the square of the normal coordinate (Castro, 2015), all leading to complex and computationally expensive algorithms. A transparent correspondence was proposed by Castro and Jansen, showing the relationships between the displacement-based formulation and the numerical implementation, where *von Kármán* and Sanders nonlinear kinematics were used for the Koiter analysis of plates (Castro and Jansen, 2021) and cylindrical shells (Castro and Jansen, 2022), respectively. Garcea et al. (1999), Garcea (2001) and Magisano et al. (2018) applied the mixed stress–displacement formulation to facilitate the construction of reduced-order models in Koiter's analysis, where both displacement and stress are degrees of freedom in the strain energy functional expression, such that the highest order non-zero variation is cubic.

The main contribution of this work is a reduced-order method for three-dimensional finite element analysis of thin-walled structures with large deformations. Two aspects make the present contribution significantly distinct from previous studies: (1) reformulating the hybrid-stress solid-shell formulations for reduced-order analysis of large deformation problems; (2) considering both the in-plane and out-of-plane large deformations of the thin-walled structures. The proposed method significantly decreases the computational cost in construction of the reduced-order model, while keeping its path-following capability and numerical accuracy for large deformation analyses, attributing to the following three reasons: (1) the fourth-order strain energy variation is naturally avoided by taking advantage of the two-field Hellinger–Reissner variational principle and the hybrid-stress solid-shell formulations; (2) the range of validity of the reduced-order solution is not decreased by recovering the third-order approximation to the equilibrium equations after applying the stress condensation; (3) the nonlinear predictor solved by the reduced system can be accurately corrected using the residual force when necessary, based on the Koiter–Newton method. Various numerical examples and one experimental validation are herein presented to demonstrate the excellent performance of the proposed method for large-deformation geometrically nonlinear analyses.

In the following, Section 2 presents the hybrid-stress solid-shell element formulations considering fully geometrical nonlinearities; the reduced-order method with hybrid-stress formulations is developed in Section 3 for large-deformation 3D finite element analysis; the proposed reduced-order method is thoroughly verified using several numerical examples in Section 4 and one experimental test in Section 5; finally, the work is summarized in Section 6.

2. The formulations of hybrid-stress solid-shell element involving geometrical nonlinearities

Fig. 1 illustrates the adopted eight-node element with three translation degrees of freedom per node. The global, local, and natural coordinate systems are constructed and denoted as $(x'$-y'-$z')$, $(x$-y-$z)$, and $(\xi$-η-$\zeta)$, respectively. The natural coordinate system ξ-η-ζ is defined at the center point of the isoparametric element, in which the axes ξ and η connect the midpoints of opposite edges of the element and the ζ-axis is along the thickness direction of the element. Note that the z-axis of the local coordinate system must be defined along the thickness direction of the solid-shell element, with $-1 \leq \xi, \eta, \zeta \leq +1$.

The coordinate x_i and displacement field U_i are linearly interpolated based on predefined shape functions N,

$$\begin{cases} x_i(\xi,\eta,\zeta) = N_{0I} x_{iI} + \zeta N_{nI} x_{iI} \\ U_i(\xi,\eta,\zeta) = N_{0I} U_{iI} + \zeta N_{nI} U_{iI} \end{cases} \quad \text{I: from 1 to 8,} \tag{1}$$

where $i = 1, 2, 3$, and Einstein's summation convention is applied to the subscript I; and,

$$\begin{cases} \mathbf{N}_0 = \frac{1}{2} \left[N_1, N_2, N_3, N_4, N_1, N_2, N_3, N_4 \right] \\ \mathbf{N}_n = \frac{1}{2} \left[N_1, N_2, N_3, N_4, -N_1, -N_2, -N_3, -N_4 \right], \end{cases} \tag{2}$$

$$N_1 = \frac{1}{4}(1-\xi)(1-\eta)$$
$$N_2 = \frac{1}{4}(1+\xi)(1-\eta)$$
$$N_3 = \frac{1}{4}(1+\xi)(1+\eta)$$
$$N_4 = \frac{1}{4}(1-\xi)(1+\eta)$$
$$\tag{3}$$

The natural displacement $\bar{U}_j$ can be represented by the local one U_i using a transformation relation based on a Jacobian matrix $\mathbf{J}$,
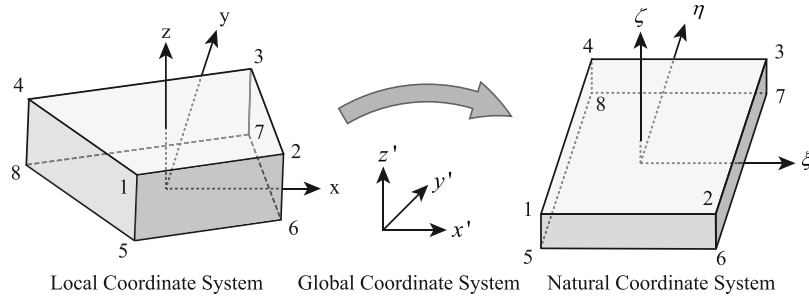
$$\bar{U}_j = J_{ij} U_i, \tag{4}$$

Fig. 1. The solid-shell element for thin-walled structures.

in which,

$$\mathbf{J} = \begin{bmatrix} \dfrac{\partial N_{0I}}{\partial \xi} x_I & \dfrac{\partial N_{0I}}{\partial \eta} x_I & 0 \\ \dfrac{\partial N_{0I}}{\partial \xi} y_I & \dfrac{\partial N_{0I}}{\partial \eta} y_I & 0 \\ 0 & 0 & N_{nI} z_I \end{bmatrix}, \tag{5}$$

In the natural coordinate system, the Green–Lagrange strain involving the fully geometrical nonlinearities becomes,

$$\bar{E}_{ij} = \frac{1}{2} \left(\frac{\partial \bar{U}_i}{\partial \xi_j} + \frac{\partial \bar{U}_j}{\partial \xi_i} + \frac{\partial \bar{U}_k}{\partial \xi_i} \frac{\partial \bar{U}_k}{\partial \xi_j} \right). \tag{6}$$

Substituting the displacement (4) into Eq. (6), the strain–displacement relationship is rewritten as,

$$\bar{\mathbf{E}} = \bar{\mathbf{B}}_l \mathbf{q} + \frac{1}{2} \bar{\mathbf{B}}_{nl}(\mathbf{q}) \mathbf{q}, \tag{7}$$

in which,

$$\bar{\mathbf{E}} = \left[\bar{E}_{\xi\xi}, \bar{E}_{\eta\eta}, 2\bar{E}_{\xi\eta}, \bar{E}_{\zeta\zeta}, 2\bar{E}_{\eta\zeta}, 2\bar{E}_{\xi\zeta} \right]^T, \tag{8}$$

where $\bar{\mathbf{B}}_l$ and $\bar{\mathbf{B}}_{nl}(\mathbf{q})$ are the linear and nonlinear interpolation matrices, respectively, and the vector $\mathbf{q}$ collects the nodal displacements U_{iI} in a column vector.

When using a three-dimensional element to model the thin-walled structures, the shear, membrane, trapezoidal, and thickness locking problems need to be overcome. For the shear and trapezoidal lockings, the natural transverse normal and shear strains of the solid-shell element are redefined using the assumed natural strain (ANS) method, as follows,

$$\begin{aligned} \bar{E}_{\zeta\zeta} &= N_1 \bar{E}_{\zeta\zeta}(1,-1,0) + N_2 \bar{E}_{\zeta\zeta}(-1,-1,0) + N_3 \bar{E}_{\zeta\zeta}(-1,1,0) \\ &\quad + N_4 \bar{E}_{\zeta\zeta}(1,1,0) \\ \bar{E}_{\eta\zeta} &= \frac{1}{2}(1-\xi)\bar{E}_{\eta\zeta}(-1,0,0) + \frac{1}{2}(1+\xi)\bar{E}_{\eta\zeta}(1,0,0) \\ \bar{E}_{\xi\zeta} &= \frac{1}{2}(1-\eta)\bar{E}_{\xi\zeta}(0,-1,0) + \frac{1}{2}(1+\eta)\bar{E}_{\xi\zeta}(0,1,0) \end{aligned} \tag{9}$$

The Green–Lagrange strain $\mathbf{E}$ presented in the local coordinate system is presented by,

$$\mathbf{E} = \mathbf{T}_\varepsilon \bar{\mathbf{E}}, \tag{10}$$

where $\mathbf{T}_\varepsilon$ is a strain transformation matrix from the natural to local coordinate systems.

The present work employs the hybrid-stress formulation to construct a modified constitutive relation for overcoming the thickness and volume lockings. As presented in the work of Pian and Sze (Pian, 1985; Sze et al., 2002), the second Piola–Kirchhoff stress $\mathbf{S}$ is given by,

$$\mathbf{S} = \begin{bmatrix} S_{xx} \\ S_{yy} \\ S_{xy} \\ S_{zz} \\ S_{yz} \\ S_{xz} \end{bmatrix} = \mathbf{T}_\sigma \begin{bmatrix} \bar{S}_{\xi\xi} \\ \bar{S}_{\eta\eta} \\ \bar{S}_{\xi\eta} \\ \bar{S}_{\zeta\zeta} \\ \bar{S}_{\eta\zeta} \\ \bar{S}_{\xi\zeta} \end{bmatrix} = \mathbf{T}_\sigma \bar{\mathbf{P}}\boldsymbol{\beta} = \mathbf{P}\boldsymbol{\beta}, \tag{11}$$

where $\mathbf{T}_\sigma$ is a stress transformation matrix from the natural to local coordinate systems, $\boldsymbol{\beta}$ is a vector with 18 stress parameters, and $\bar{\mathbf{P}}$ and $\mathbf{P}$ are predefined stress interpolation matrices in the natural and local coordinate systems, respectively.

Then, the Green–Lagrange strain $\mathbf{E}$ and the second Piola–Kirchhoff stress $\mathbf{S}$ described in the local coordinate system are summarized to be,

$$\mathbf{E} = \mathbf{B}_l \mathbf{q} + \frac{1}{2} \mathbf{B}_{nl}(\mathbf{q})\mathbf{q}, \tag{12}$$

$$\mathbf{S} = \mathbf{P}\boldsymbol{\beta}, \tag{13}$$

where $\mathbf{P}$, $\mathbf{B}_l$, and $\mathbf{B}_{nl}$ are the stress interpolation matrix, the linear and nonlinear interpolation matrices, respectively, which are defined in the local coordinate system.

After truncating the second-order terms of ζ in the in-plane strain $\mathbf{E}_p$, the Green–Lagrange strain $\mathbf{E}$ is reformulated as,

$$\mathbf{E} = \begin{bmatrix} \mathbf{E}_p \\ E_z \\ \mathbf{E}_t \end{bmatrix} = \begin{bmatrix} \mathbf{E}_m + \zeta \mathbf{E}_b \\ E_z \\ \mathbf{E}_t \end{bmatrix} = \begin{bmatrix} \mathbf{B}_{lm} + \frac{1}{2}\mathbf{B}_{nlm}(\mathbf{q}) + \zeta[\mathbf{B}_{lb} + \frac{1}{2}\mathbf{B}_{nlb}(\mathbf{q})] \\ \mathbf{B}_{lz} + \frac{1}{2}\mathbf{B}_{nlz}(\mathbf{q}) \\ \mathbf{B}_{lt} + \frac{1}{2}\mathbf{B}_{nlt}(\mathbf{q}) \end{bmatrix}, \tag{14}$$

where the components $\mathbf{E}_p$, E_z, and $\mathbf{E}_t$ denote the in-plane, transverse normal, and transverse shear strains, respectively.

Correspondingly, the second Piola–Kirchhoff stress $\mathbf{S}$ in (13) is also rewritten as,

$$\mathbf{S} = \begin{bmatrix} \mathbf{S}_p \\ S_z \\ \mathbf{S}_t \end{bmatrix} = \begin{bmatrix} \mathbf{P}_p \\ \mathbf{P}_z \\ \mathbf{P}_t \end{bmatrix} \boldsymbol{\beta}. \tag{15}$$

Then, the three-dimensional constitutive equations become,

$$\mathbf{E} = \mathbf{C}^{-1}\mathbf{S}$$
$$\Rightarrow \begin{bmatrix} \mathbf{E}_p \\ E_z \\ \mathbf{E}_t \end{bmatrix} = \begin{bmatrix} \mathbf{F}_{pp} & \mathbf{F}_{pz} & \mathbf{0} \\ \mathbf{F}_{pz}^T & F_{zz} & \mathbf{0} \\ \mathbf{0} & \mathbf{0} & \mathbf{F}_t \end{bmatrix} \begin{bmatrix} \mathbf{S}_p \\ S_z \\ \mathbf{S}_t \end{bmatrix}, \tag{16}$$

where $\mathbf{C}^{-1}$ denotes the flexibility matrix. Note that the strain $\mathbf{E}$ derived by the constitutive equations is not exactly the Green–Lagrange strain (12), however the product of the strain and the second Piola–Kirchhoff stress should be equal to the product of the Green–Lagrange strain and the second Piola–Kirchhoff stress on an integral domain of the solid-shell element.

The thickness and volume lockings are eliminated by assuming the thickness stress S_z be independent of ζ. Using the relation $\mathbf{E}_p = \mathbf{E}_m + \zeta\mathbf{E}_b$ in Eq. (14) and extracting the terms related to ζ, the constitutive equations (16) can be reformulated to be,

$$\begin{bmatrix} \mathbf{S}_p \\ E_z \\ \zeta\mathbf{S}_p \end{bmatrix} = \begin{bmatrix} \mathbf{A} & \mathbf{B} & \zeta\mathbf{A} \\ -\mathbf{B}^T & D & -\zeta\mathbf{B}^T \\ \zeta\mathbf{A} & \zeta\mathbf{B} & \zeta^2\mathbf{A} \end{bmatrix} \begin{bmatrix} \mathbf{E}_m \\ S_z \\ \mathbf{E}_b \end{bmatrix}, \tag{17}$$

in which,

$$\mathbf{A} = \mathbf{F}_{pp}^{-1}, \mathbf{B} = -\mathbf{F}_{pp}^{-1}\mathbf{F}_{pz}, D = F_{zz} - \mathbf{F}_{pz}^T\mathbf{F}_{pp}^{-1}\mathbf{F}_{pz}. \tag{18}$$

After applying the pre-integrating along the ζ direction for the constitutive equations (17), a modified constitutive relation is achieved.

Then, the strain energy of the solid-shell element is presented to be a two-field (displacement and stress) form,

$$U = \int_V \left(-\frac{1}{2} \mathbf{S}^T \mathbf{C}^{-1} \mathbf{S} + \mathbf{S}^T \mathbf{E} \right) dV = -\frac{1}{2} \boldsymbol{\beta}^T \mathbf{H} \boldsymbol{\beta} + \boldsymbol{\beta}^T (\mathbf{G}_l + \frac{1}{2} \mathbf{G}_{nl}(\mathbf{q})) \mathbf{q}, \quad (19)$$

in which,

$$\mathbf{H} = \int_V \mathbf{P}^T \mathbf{C}^{-1} \mathbf{P} \, dV, \tag{20}$$

$$\mathbf{G}_l = \int_V \mathbf{P}^T \mathbf{B}_l \, dV, \tag{21}$$

$$\mathbf{G}_{nl} = \int_V \mathbf{P}^T \mathbf{B}_{nl} \, dV, \tag{22}$$

where the modified constitutive relation is involved in the calculation of $\mathbf{H}$ in Eq. (20).

3. Reduced-order method with hybrid-stress formulations for large deformation analysis

The total potential energy Π of the structure is written to be a Hellinger–Reissner functional,

$$\Pi = -\frac{1}{2} \boldsymbol{\beta}^T \mathbf{H} \boldsymbol{\beta} + \boldsymbol{\beta}^T (\mathbf{G}_l + \frac{1}{2} \mathbf{G}_{nl}(\mathbf{q})) \mathbf{q} - \mathbf{q}^T (\lambda \mathbf{f}_{ext}), \tag{23}$$

where $\mathbf{f}_{ext}$ is the external load and its corresponding load multiplier is denoted by λ.

The geometrically nonlinear equilibrium equations can be achieved using the two-field variational principle and minimum potential energy principle,

$$-\mathbf{H}\boldsymbol{\beta} + \left[\mathbf{G}_l + \frac{1}{2} \mathbf{G}_{nl}(\mathbf{q}) \right] \mathbf{q} = \mathbf{0}, \tag{24a}$$

$$\left[\mathbf{G}_l + \mathbf{G}_{nl}(\mathbf{q}) \right]^T \boldsymbol{\beta} = \lambda \mathbf{f}_{ext}, \tag{24b}$$

where the Hellinger–Reissner functional (23) is stationary at the equilibrium for any variations of $\mathbf{q}$ and $\boldsymbol{\beta}$. Therefore, Eq. (24a) comes from the variation of $\boldsymbol{\beta}$, whereas Eq. (24b) from the variation of $\mathbf{q}$.

The nonlinear equilibrium equations (24a) and (24b) with two parameters are represented by a more general form,

$$\mathbf{f}(\boldsymbol{\beta}, \mathbf{q}) = \lambda \mathbf{f}_{ext}, \tag{25}$$

where the internal force $\mathbf{f}$ is functionally related to the two unknown parameter vectors of displacement $\mathbf{q}$ and stress $\boldsymbol{\beta}$. In our work, the conventional finite element method based on the Newton–Raphson technique is referred to as the full-order method with N degrees of freedom.

Similarly to the conventional finite element method (full-order method), the proposed reduced-order method traces the geometrically nonlinear response of the structure in a step-by-step manner for the path-following analysis. In each path-following step, a novel predictor–corrector strategy is applied by using the solution of the reduced-order model as a nonlinear predictor, and consecutive Newton iterations as the correctors, as detailed next.

3.1. Nonlinear predictor obtained by the reduced-order model

In each path-following step, the reduced-order model is constructed at a known equilibrium configuration$(\boldsymbol{\beta}_0, \mathbf{q}_0, \lambda_0)$, to approximate the geometrically nonlinear equilibrium given by Eq. (25). For the first step, the already known configuration must be the undeformed configuration $(\boldsymbol{\beta}_0 = \mathbf{0}, \mathbf{q}_0 = \mathbf{0}, \lambda_0 = 0)$. Then, the unknown configuration is obtained by,

$$\boldsymbol{\beta} = \boldsymbol{\beta}_0 + \Delta\boldsymbol{\beta}, \tag{26}$$

$$\mathbf{q} = \mathbf{q}_0 + \Delta\mathbf{q}, \tag{27}$$

$$\lambda = \lambda_0 + \Delta\lambda, \tag{28}$$

where $\Delta\boldsymbol{\beta}$, $\Delta\mathbf{q}$, and $\Delta\lambda$ are the increments of the three variables varying from the known to unknown configurations, respectively.

Substituting Eqs. (26), (27), and (28) into Eq. (25), the nonlinear equilibrium equations (25) in a two-field form are represented to be a third-order Taylor's expansion,

$$\mathbf{f}'(\boldsymbol{\beta}_0, \mathbf{q}_0, \Delta\boldsymbol{\beta}, \Delta\mathbf{q}) + \mathbf{f}^{(2)}(\boldsymbol{\beta}_0, \mathbf{q}_0, \Delta\boldsymbol{\beta}^2, \Delta\mathbf{q}^2) + \mathbf{f}^{(3)}(\boldsymbol{\beta}_0, \mathbf{q}_0, \Delta\boldsymbol{\beta}^3, \Delta\mathbf{q}^3)$$
$$+ \mathbf{O}(\boldsymbol{\beta}_0, \mathbf{q}_0, \|\Delta\boldsymbol{\beta}\|^4, \|\Delta\mathbf{q}\|^4) = \Delta\lambda\mathbf{f}_{ext}, \tag{29}$$

where the equilibrium condition $\mathbf{f}(\boldsymbol{\beta}_0, \mathbf{q}_0) = \lambda_0 \mathbf{f}_{ext}$ at the already known configuration is applied; and $\mathbf{f}'$, $\mathbf{f}^{(2)}$, $\mathbf{f}^{(3)}$, and $\mathbf{O}$ denote the linear, quadratic, cubic, and higher-order terms of the Taylor's equation, respectively. The determination of operators $\mathbf{f}'$, $\mathbf{f}^{(2)}$, $\mathbf{f}^{(3)}$ requires the second to fourth-order variations of the strain energy U in (19) with respect to the degrees of freedom related to displacement $\mathbf{q}$ and stress $\boldsymbol{\beta}$, as follows,

$$\delta^2 U = \left\{ \delta\boldsymbol{\beta}^T \quad \delta\mathbf{q}^T \right\} \begin{bmatrix} -\mathbf{H} & [\mathbf{G}_l + \mathbf{G}_{nl}(\mathbf{q})] \\ [\mathbf{G}_l + \mathbf{G}_{nl}(\mathbf{q})]^T & \mathbf{G}_{nl}^T \boldsymbol{\beta} \end{bmatrix} \left\{ \begin{matrix} \delta\boldsymbol{\beta} \\ \delta\mathbf{q} \end{matrix} \right\}, \tag{30}$$

$$\delta^3 U = \left\{ \delta\boldsymbol{\beta}^T \quad \delta\mathbf{q}^T \right\} \begin{bmatrix} \mathbf{0} & \mathbf{G}_{nl}\delta\mathbf{q} \\ \mathbf{G}_{nl}^T(\delta\mathbf{q}) & \mathbf{G}_{nl}^T\delta\boldsymbol{\beta} \end{bmatrix} \left\{ \begin{matrix} \delta\boldsymbol{\beta} \\ \delta\mathbf{q} \end{matrix} \right\}, \tag{31}$$

$$\delta^4 U = 0, \tag{32}$$

with the fourth-order strain energy variation $\delta^4 U$ being zero, given that the strain energy (23) has a third-order polynomial dependence in both the displacement and stress. Therefore, the third-order term $\mathbf{f}^{(3)}$ in (29) vanishes, making the nonlinear equilibrium equations depend only with second order on the degrees of freedom, simplifying the construction of the reduced-order model. In displacement-based formulations (Liang et al., 2013, 2014), the fourth-order dependency on the degrees of freedom leads to immense computational costs.

Substituting the high-order strain energy variations (30), (31), and (32) into the equilibrium equations (29), and condensing the stress parameter $\boldsymbol{\beta}$, the nonlinear equilibrium equations can be reformulated to be a third-order form involving only the displacement $\mathbf{q}$,

$$\mathbf{L}(\Delta\mathbf{q}) + \mathbf{Q}(\Delta\mathbf{q}, \Delta\mathbf{q}) + \mathbf{C}(\Delta\mathbf{q}, \Delta\mathbf{q}, \Delta\mathbf{q}) = \Delta\lambda\mathbf{f}_{ext}, \tag{33}$$

in which,

$$\mathbf{L}(\Delta\mathbf{q}) = \left\{ \left[\mathbf{G}_l + \mathbf{G}_{nl}(\mathbf{q}_0) \right]^T \mathbf{H}^{-1} \left[\mathbf{G}_l + \mathbf{G}_{nl}(\mathbf{q}_0) \right] \right.$$
$$\left. + \mathbf{q}_0^T \left[\mathbf{G}_l + \frac{1}{2} \mathbf{G}_{nl}(\mathbf{q}_0) \right]^T \mathbf{H}^{-1} \mathbf{G}_{nl} \right\} \Delta\mathbf{q}, \tag{34}$$

$$\mathbf{Q}(\Delta\mathbf{q}, \Delta\mathbf{q}) = \frac{1}{2} \left[\mathbf{G}_l + \mathbf{G}_{nl}(\mathbf{q}_0) \right]^T \mathbf{H}^{-1} \mathbf{G}_{nl}(\Delta\mathbf{q})\Delta\mathbf{q} + \frac{1}{2}\Delta\mathbf{q}^T \left[\mathbf{G}_l + \mathbf{G}_{nl}(\mathbf{q}_0) \right]^T$$
$$\times \mathbf{H}^{-1} \mathbf{G}_{nl}\Delta\mathbf{q} \tag{35}$$
$$+ \frac{1}{2}\Delta\mathbf{q}^T (\mathbf{G}_{nl})^T \mathbf{H}^{-1} \left[\mathbf{G}_l + \mathbf{G}_{nl}(\mathbf{q}_0) \right] \Delta\mathbf{q}, \tag{36}$$

$$\mathbf{C}(\Delta\mathbf{q}, \Delta\mathbf{q}, \Delta\mathbf{q}) = \frac{1}{4} \left[\mathbf{G}_{nl}(\Delta\mathbf{q})\Delta\mathbf{q} \right]^T \mathbf{H}^{-1} \mathbf{G}_{nl}\Delta\mathbf{q} + \frac{1}{4} \left[\mathbf{G}_{nl}(\Delta\mathbf{q}) \right]^T \mathbf{H}^{-1} \mathbf{G}_{nl}(\Delta\mathbf{q})\Delta\mathbf{q}, \tag{37}$$

where the third-order approximation to equilibrium equations is again recovered by condensing the stress.

Analogously, the increments of the load multiplier $\Delta\lambda$ and displacement $\Delta\mathbf{q}$ are expanded to be a third-order form with respective to the generalized displacement ξ,

$$\Delta\lambda = \bar{L}\xi + \bar{Q}\xi^2 + \bar{C}\xi^3 + \mathbf{O}(\xi^4), \tag{38}$$

$$\Delta\mathbf{q} = \mathbf{u}_L\xi + \mathbf{u}_Q\xi^2 + \mathbf{u}_C\xi^3 + \mathbf{O}(\xi^4), \tag{39}$$

where $\bar{L}$, $\bar{Q}$, and $\bar{C}$ denote the, still to be determined, first to third-order coefficients of the load multiplier $\Delta\lambda$, respectively, and $\mathbf{u}_L$, $\mathbf{u}_Q$, and $\mathbf{u}_C$ are the, still to be determined, first to third-order bases of the displacement increment $\Delta\mathbf{q}$, respectively. The first-order displacement field $\mathbf{u}_L$ defines a tangent plane to the equilibrium surface at the already known configuration, whereas $\mathbf{u}_Q$ and $\mathbf{u}_C$ are the second- and third-order displacement fields.

Substituting the increments of the load multiplier $\Delta\lambda$ (38) and displacement $\Delta\mathbf{q}$ (39) into both sides of the nonlinear equilibrium equations (33) and equating the coefficients of the various powers of ξ to zero, two linear systems of equations and one algebraic equation are obtained,

$$\begin{bmatrix} \mathbf{L} & -\mathbf{f}_{ext} \\ -\mathbf{f}_{ext}^T & 0 \end{bmatrix} \begin{Bmatrix} \mathbf{u}_L \\ \bar{L} \end{Bmatrix} = \begin{Bmatrix} \mathbf{0} \\ -1 \end{Bmatrix}, \tag{40}$$

$$\begin{bmatrix} \mathbf{L} & -\mathbf{f}_{ext} \\ -\mathbf{f}_{ext}^T & 0 \end{bmatrix} \begin{Bmatrix} \mathbf{u}_Q \\ \bar{Q} \end{Bmatrix} = \begin{Bmatrix} -\mathbf{Q}(\mathbf{u}_L, \mathbf{u}_L) \\ 0 \end{Bmatrix}, \tag{41}$$

$$\bar{C} = -2\mathbf{u}_Q^T \mathbf{L}(\mathbf{u}_Q) + \mathbf{u}_L^T \mathbf{C}(\mathbf{u}_L, \mathbf{u}_L, \mathbf{u}_L), \tag{42}$$

where the two linear systems (40) and (41) have the identical coefficient matrix with a order of N+1, thus only one matrix factorization is required. Eqs. (40), (41), and (42) are then solved to obtain the values of $\bar{L}$, $\bar{Q}$, $\bar{C}$, $\mathbf{u}_L$, and $\mathbf{u}_Q$.

Up to this point, the reduced-order model that can approximate the geometrically nonlinear equilibrium equations (25) at the already known configuration is constructed, given by,

$$\bar{L}\xi + \bar{Q}\xi^2 + \bar{C}\xi^3 = \Delta\lambda, \tag{43}$$

which is a nonlinear equation having only one degree of freedom. The relation between ξ and $\Delta\lambda$ is obtained by continuously changing the value of $\Delta\lambda$. With Eqs. (27), (28), and (39), the solution about ($\mathbf{q}$ vs. λ) is achieved and regarded as a nonlinear predictor to the geometrically nonlinear response of the structure undergoing large deformations.

3.2. Corrector phase based on the residual force

The range of validity of the reduced system (43) is limited, gradually deviating from the geometrically nonlinear response away from the expansion point. This range of validity can be determined based on the residual force and the external load, as given by,

$$\frac{\|\mathbf{f}_{res}\|}{\lambda\|\mathbf{f}_{ext}\|} < \epsilon, \tag{44}$$

in which,

$$\mathbf{f}_{res} = \lambda\mathbf{f}_{ext} - \mathbf{f}(\mathbf{q}), \tag{45}$$

where the residual force $\mathbf{f}_{res}$ is obtained by taking the internal force $\mathbf{f}(\mathbf{q})$ from the external load $\lambda\mathbf{f}_{ext}$, and ϵ is a predefined error threshold. When the criterion (45) is not satisfied, a corrector phase is applied to drive the residual $\mathbf{f}_{res}$ towards zero, similarly to traditional Newton-based iteration methods. Here, the Newton iteration process is conducted using the full-order finite element model, thereby guaranteeing the accuracy of the correction phase. After correction, a new equilibrium configuration is achieved, and a full path-following step with a predictor–corrector strategy is completed, and it can be repeated multiple times to further advance the nonlinear analysis.

4. Numerical examples

Benchmark structures undergoing large deflection, large rotation, and large strain; are studied to evaluate the computational capability of the proposed method. First, we investigate three rectangular plates subjected to out-of-plane shear, bending and in-plane tensile loads, respectively. Next, a honeycomb cell under in-plane loads and a swept-back wingbox under out-of-plane loads are studied, both representing structures with complex geometry.
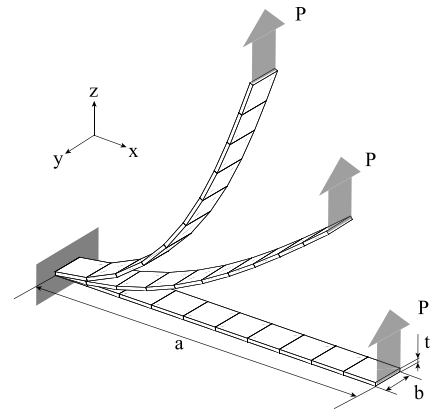

Fig. 2. The cantilevered plate subjected to end shear load.

4.1. Rectangular plates subjected to in-plane and out-of-plane loads

4.1.1. Slender plate under end shear load (large deflection problem)

As shown in Fig. 2, the geometrical parameters of the slender cantilever plate are: length $a = 100$ mm, width $b = 10$ mm and thickness $t = 1$ mm. The properties of the selected isotropic material are $E = 12\,000$ MPa and $\mu = 0$. The left end of the plate is fixed, while a vertical shear load of $P = 5$ N is uniformly applied to the right end. The deflection-span ratio of the plate is designed to be roughly 70%, making it a severe test for the proposed method. Ten hexahedral elements with a large span-thickness ratio of 10:1 are used along the length of the plate.

First, the geometrically nonlinear responses of the structure are calculated and compared using different full-order finite element methods, which are ABAQUS with four commonly used three-dimensional elements (C3D8I, C3D8R, CSS8, and SC8R) and the full-order method using the proposed hybrid-stress solid-shell formulation, herein referred to as FOM. The classical Newton–Raphson method is applied to all the full-order finite element methods, including ABAQUS.

The average displacements in the horizontal (x) and vertical (z) directions are counted along all the nodes at the right end of the plate, and the corresponding load–displacement curves are plotted in Fig. 3. It is shown that the geometrically nonlinear responses obtained by ABAQUS' elements CSS8 (8-node linear brick solid-shell, incompatible modes, with assumed strain) and SC8R (8-node quadrilateral continuum shell) coincide exactly with each other. The results of C3D8I element (8-node linear brick, incompatible modes) gradually deviate from those of CSS8 and SC8R as the external load increases, but still exhibit the same nonlinear characteristics. However, the C3D8R element (8-node linear brick, reduced integration, hourglass control) leads to a completely wrong solution, in which a much lower structural stiffness is obtained even at the undeformed configuration $p = 0$ N, indicating that the C3D8R element with a large span-thickness ratio of 10:1 meets the numerical locking problems. The results obtained with FOM are in good agreement with ABAQUS' CSS8 and SC8R elements.

Then, the reduced-order method (ROM) using hybrid-stress solid-shell formulations is applied to obtain the geometrically nonlinear responses of the plate. As shown in Fig. 4, the response curves obtained by the ROM using three path-following steps are in good agreement with the exact solutions of the FOM, both for the horizontal and the vertical displacements. For the sake of clarity, each dotted symbol (•) in Fig. 4 includes three path-following steps of the FOM, because the FOM with multiple steps results in a large number of solution points along the response curve. Each step size of the ROM is represented by the circle symbol (○). The smoothness of the response curve obtained by the ROM is obtained with more solution points added at small intervals, without affecting the computational cost. Note from Fig. 4 that the step
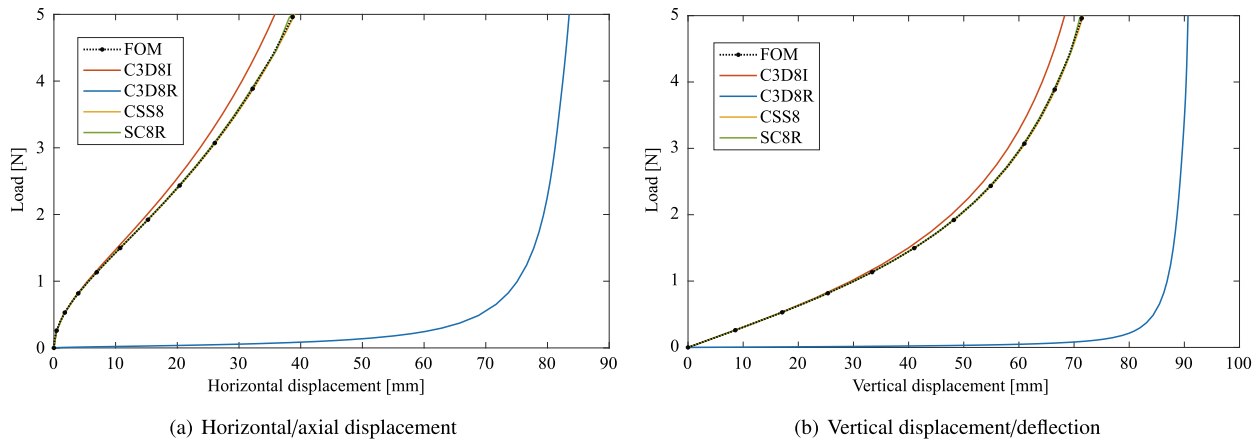
(a) Horizontal/axial displacement

(b) Vertical displacement/deflection

Fig. 3. Geometrically nonlinear responses of the slender plate under end shear load, obtained by ABAQUS with four different elements and the full-order method of our in-house codes.
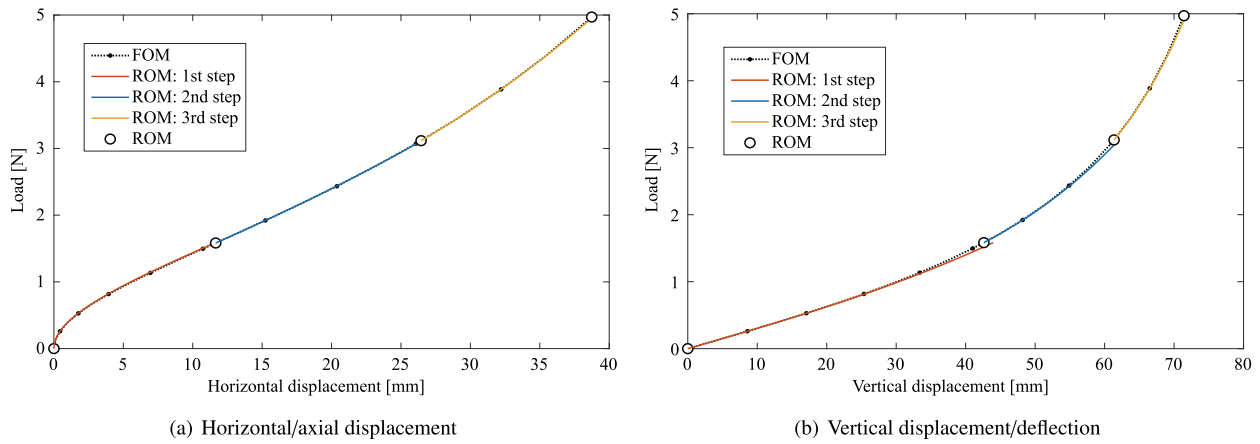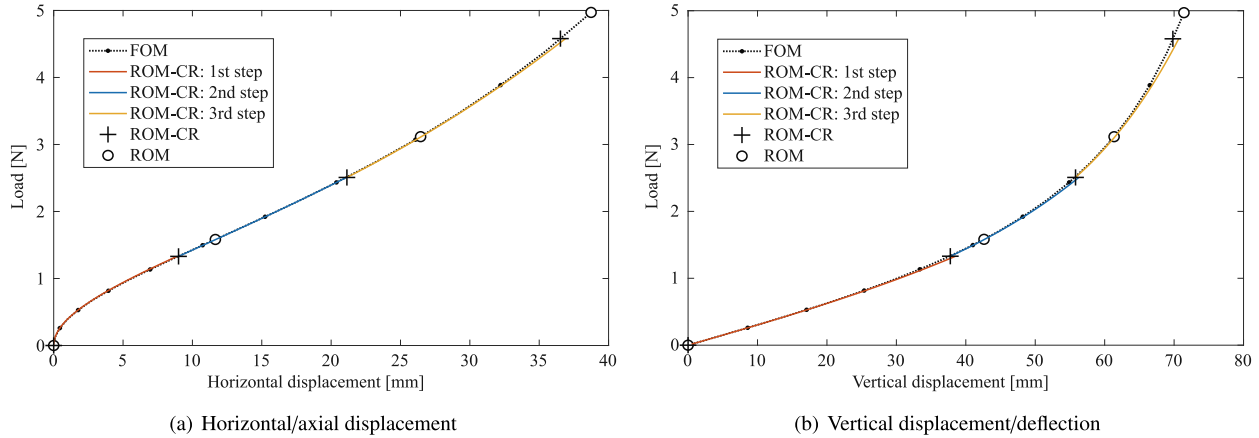

(a) Horizontal/axial displacement

(b) Vertical displacement/deflection

Fig. 4. Geometrically nonlinear responses of the slender plate under end shear load, obtained by the reduced-order method.
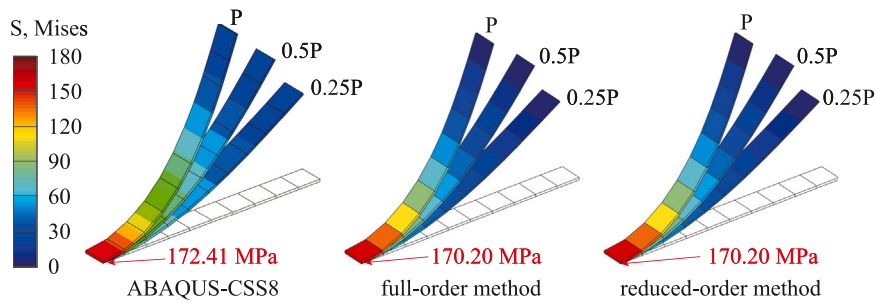
Fig. 5. The von Mises stress colored by the magnitude of the stress vector, for the slender plate under end shear load.

size of a single path-following step of the ROM is equivalent to that of 7–13 steps of the FOM, demonstrating that the ROM using hybrid-stress solid-shell formulation can accurately and efficiently trace the geometrically nonlinear responses.

The deformed state of the cantilever slender plate obtained with ABAQUS, FOM and ROM are compared in Fig. 5 for three different load levels: 0.25 P, 0.5 P and 1.0 P. The distribution of the von Mises stress is also plotted. A good agreement with ABAQUS is obtained for both the FOM and ROM.

Next, we assess the number of path-following steps and iterations required by ABAQUS, with four different elements, the FOM, and ROM. The results are compared in Table 1. The C3D8I, CSS8, and SC8R elements of ABAQUS adopts 32 path-following steps and 88 iterations on average (excluding C3D8R that rendered incorrect solutions), while

the FOM requires 30 steps and 89 iterations. The ROM requires only three steps and 17 iterations. Solutions to the same nonlinear problem presented in the literature are also listed in Table 1. Sze et al. (2004) adopted the ABAQUS shell elements and used 15 path-following steps with 90 iterations; whereas 9 steps with 43 iterations are taken by Rong et al. (2022) using the modified unified co-rotational shell framework.

Finally, the reduced-order method using co-rotational shell formulations (ROM-CR) is used for geometrically nonlinear analysis, which can be regarded as the reduced-order method using displacement-based formulations. As shown in Fig. 6, the results of the ROM-CR are also in good agreement with the exact results of FOM, and only three path-following steps are needed to obtain the geometrically nonlinear responses. The step sizes of the ROM-CR and ROM are respectively indicated by the cross (+) and circle (∘) symbols. The exact number

Table 1

Number of path-following steps and iterations required by different methods, for the slender plate under end shear load.

Methods	ABAQUS				Literatures		In-house codes	
	C3D8I	C3D8R	CSS8	SC8R	Sze	Rong	FOM	ROM
Number of path-following steps	30	55	34	31	15	9	30	3
Number of iterations	80	207	92	91	90	43	89	17

(a) Horizontal/axial displacement

(b) Vertical displacement/deflection

Fig. 6. Geometrically nonlinear responses of the slender plate under end shear loads, obtained by the reduced-order method using displacement-based co-rotational shell formulations.

Table 2

Comparison of the step size for path-following analysis using the full- and reduced-order methods, for the slender plate under end shear load.

Methods	Step 1	Step 2	Step 3
Reduced-order method using displacement-based formulation (ROM-CR)	1	1	1
Number of steps for full-order method	13	7	8
Reduced-order method (ROM) using hybrid-stress solid-shell formulations	1	1	1
Number of steps for full-order method	15	9	6

Fig. 7. The cantilevered plate subjected to end bending moment.

of full-order steps corresponding to each path-following step of the two reduced-order methods is shown in Table 2, demonstrating that the proposed ROM leads to a larger step size than the displacement-based formulation of the ROM-CR. Besides the demonstrated superior path-following capability of the proposed ROM when compared to the displacement-based ROM-CR, the constructional time for each reduced-order model is 0.15 s when using the hybrid-stress formulation, which is much less than the 15 s taken by the displacement-based formulations.

4.1.2. Slender plate under end bending moment (large rotation problem)

The classical large-rotation example of a cantilever plate subjected to an end bending moment is illustrated in Fig. 7. The geometrical parameters are: length $a = 120$ mm, width $b = 10$ mm, and thickness $t = 1$ mm. The isotropic material parameters remain the same as those used in Sections Section 4.1.1. The left end of the plate is fixed, while a bending moment of $M = 550$ N m is applied to the right end. The rectangular plate is represented by twelve hexahedral elements with a large span-thickness ratio of 10:1.

First, the geometrically nonlinear responses obtained by different full-order finite element methods are plotted in Fig. 8. Among them, the results obtained by CSS8 element of ABAQUS agrees best with those of the proposed FOM. A more apparent discrepancy in horizontal displacement appears when the bending moment M exceeds 400 N m,
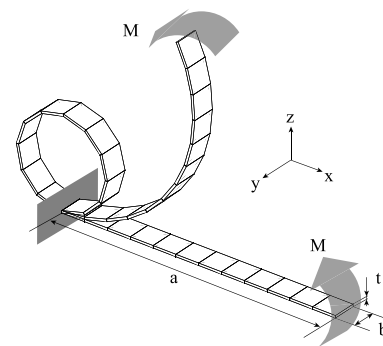
due to the increased rotational deformation and geometrical nonlinearity of the plate, which is probably a result of the different total or updated Lagrange formulations used for the FOM and the CSS8, respectively. It is also observed that the SC8R element give exactly the same results as the CSS8 when $M \leq 200$ N m; however, after that point, the path-following process for the SC8R is interrupted due to an excessive number of iterations. The results of C3D8R is completely wrong right from the beginning of the geometrically nonlinear analysis.

Then, the proposed ROM is employed for the geometrically nonlinear analysis, as shown in Fig. 9. Each path-following step of the ROM is distinguished by the response curve with a different color, and the corresponding step sizes are indicated using the circle symbol (○). Note that each dotted symbol (•) indicates three path-following steps of the FOM. The results obtained by the ROM using 11 path-following steps are in good agreement with the exact results of the FOM using 100 steps.

The rotational deformations of the slender plate colored by the magnitude of the displacement vector are plotted in Fig. 10, which are obtained by different methods. The deformed configurations at the load levels of 0.25 M, 0.5 M and 1.0 M, show the transition process of the plate deformed from its initial configuration to the fully curled configuration.

Finally, the required number of path-following steps and iterations are compared in Table 3. The ROM required 11 steps and 110 iterations,
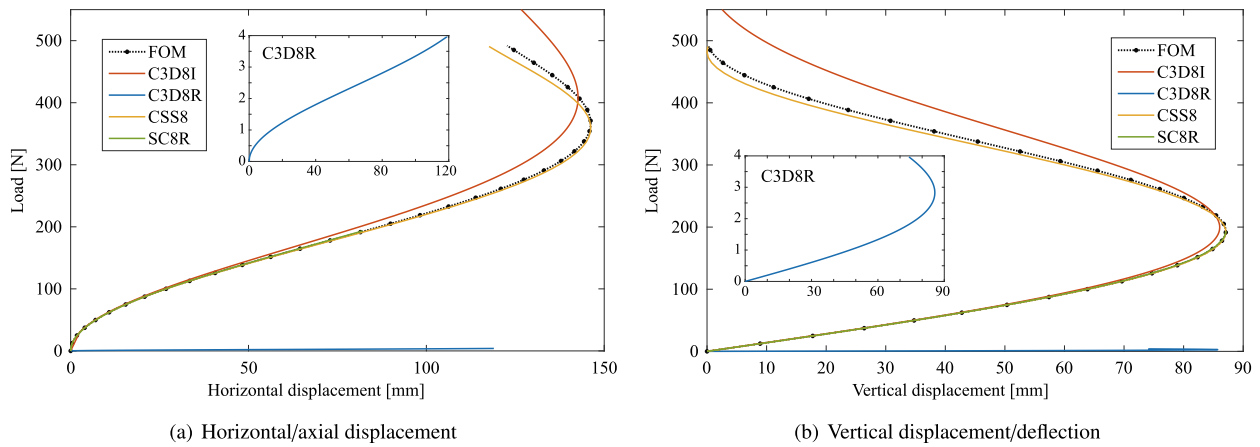
(a) Horizontal/axial displacement

(b) Vertical displacement/deflection

Fig. 8. Geometrically nonlinear responses of the slender plate under end bending moment, obtained by ABAQUS with four different elements and the full-order method of our in-house codes.
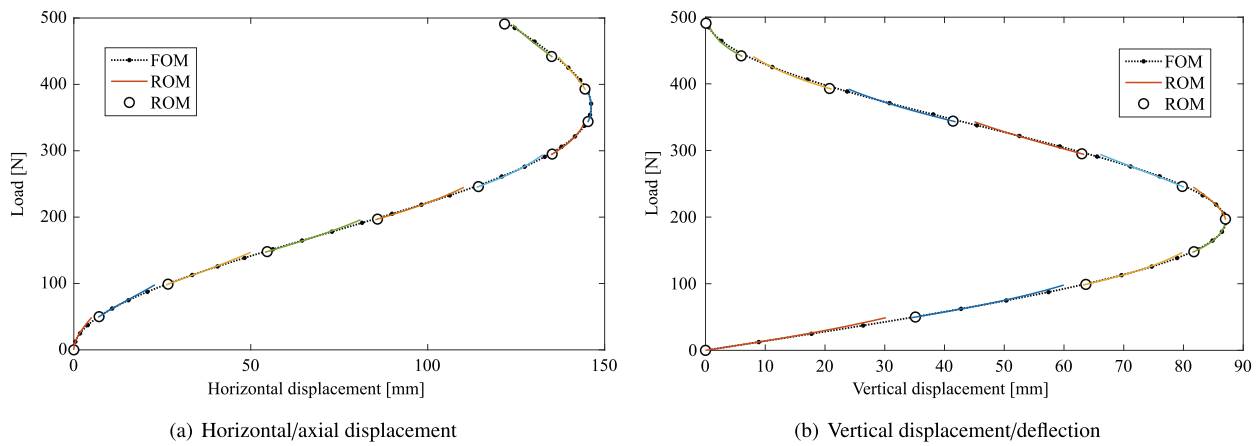

(a) Horizontal/axial displacement

(b) Vertical displacement/deflection

Fig. 9. Geometrically nonlinear responses of the slender plate under end bending moment, obtained by the reduced-order method.
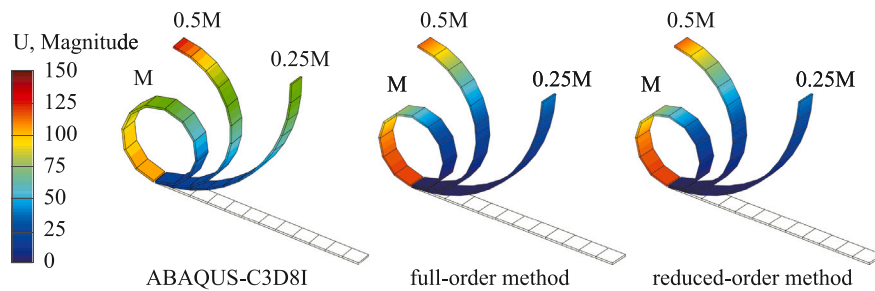
Fig. 10. Deformed configurations colored by the magnitude of the displacement vector, for the slender plate under end bending moment.

Table 3
Number of path-following steps and iterations required by different methods, for the slender plate under end bending moment.

Methods	ABAQUS				Literatures		In-house codes	
	C3D8I	C3D8R	CSS8	SC8R	Sze	Rong	FOM	ROM
Number of path-following steps	195	300	61	31	80	16	100	11
Number of iterations	1011	2000	363	238	NaN	158	407	110

while providing a smooth nonlinear response. The FOM required 100 steps and 407 iterations. ABAQUS' C3D8I has the highest computational cost with 195 steps and 1011 iterations, whereas the CSS8 used 61 steps and 363 iterations. The C3D8R and SC8R are not included in the comparison, given their poor accuracy. Although only 16 steps are required by Rong et al. (2022), the smoothness of the response curve much be rather bad.

4.1.3. Plate under end tensile load (large strain problem)

As shown in Fig. 11, a rectangular plate subjected to an in-plane tensile load is selected to examine the computational ability of the proposed method for large strain problems. The geometrical parameters of the plate are: length $a = 100$ mm, width $b = 50$ mm, and thickness $t = 1$ mm. The isotropic material parameters remain the same as those used in Sections 4.1.1 and 4.1.2. The left end of the plate is
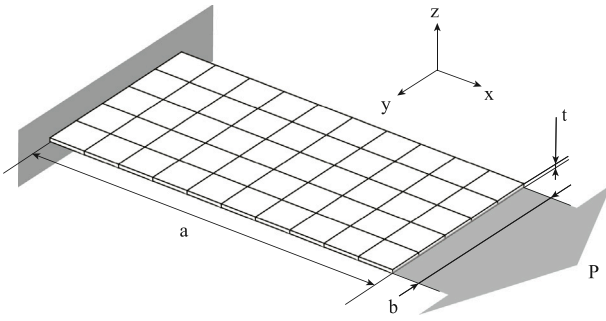
Fig. 11. The cantilevered plate subjected to end tensile load.
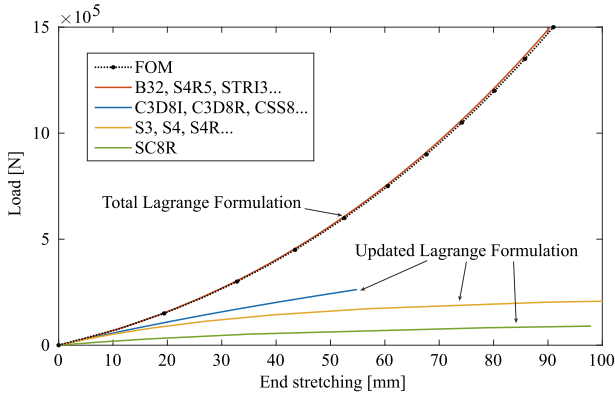

Fig. 12. Geometrically nonlinear responses of the stretched plate, obtained by ABAQUS with different elements and the full-order method of our in-house codes.

fixed, while a tensile load of $P = 1500$ kN is applied horizontally and uniformly to the right end. A 90% strain is achieved, and material nonlinearities are ignored. The rectangular plate is represented by 10, 5 and 1 elements along the length, width and thickness directions of the plate, respectively; as shown in Fig. 11. A large span-thickness ratio of 10:1 is applied to each 3D element.

First, the proposed FOM is compared against various commonly used elements from ABAQUS: one-dimensional (1D) beam, two-dimensional (2D) shell, and three-dimensional (3D) solid. The results in Fig. 12 show that the response curves obtained by the different methods can be categorized into two groups, according to the different Lagrange formulations used in the nonlinear analysis. The B32 and B33 (1-D beam elements), STRI3 and STRI65 (2-D triangular elements), and S4R5, S8R, S8R5 (2-D quadrilateral elements) all adopt the total Lagrange formulation; hence roughly the same response curves are obtained by ABAQUS, showing a stiffness-hardening phenomenon with the increase of the tensile load. The solution of the proposed FOM matches very well with these solutions, because the total Lagrange formulation is also adopted in this work. However, for the C3D8, C3D8H, C3D8I, C3D8R, C3D8S, SC8R, and CSS8 (3D hexahedral solid elements) and S3, S4, and S4R (2D shell elements), the response curves are quite different to each other but all exhibit a stiffness-softening behavior, since the updated Lagrange formulation is applied to these elements. The discrepancy in these stiffness-softening response curves mainly comes from the differences in element type and mesh convergence behavior.

Then, the proposed FOM and ROM are compared in Fig. 13, where each dotted symbol (•) indicates three steps of the FOM, while the step sizes of the ROM are indicated by the circle symbol (○). Fig. 13(a) shows the response curve obtained by the ROM using only one path-following step, exhibiting the same nonlinear characteristics as that of the FOM. To accurately obtain the geometrically nonlinear responses

up to the load of 1500 kN, a correction phase is initiated at the load of 500 kN followed by the second path-following step, as shown in Fig. 13(b), leading to a better agreement with the FOM. An average of 30 path-following steps and 45 iterations is required by different full-order methods to obtain the geometrically nonlinear responses up to the load of 1500 kN.

As a summary of the three examples of rectangular plates presented in Section 4.1, the CPU running times of the full- (FOM) and reduced-order methods (ROM) using hybrid-stress solid-shell formulations are shown in Table 4, and compared with that of ABAQUS. Note that the computer with an i7-CPU, eight processors, and 32 GB of RAM is used to test the computational efficiency of different methods, and only ABAQUS' elements that resulted on the same solution as the proposed FOM are included. The computational efficiency of the proposed ROM using the hybrid-stress solid-shell formulation is confirmed. It should be mentioned that for the large rotational case, the advantage of the proposed ROM in computational efficiency is not as obvious as that for the other two cases (large deflection and strain). The reason is that when geometrical nonlinearity is extremely significant, the ROM requires more path-following steps, leading to more computational cost in the construction of reduced-order models.

4.2. Structures with complex geometrical shapes subjected to in-plane and out-of-plane loads

4.2.1. Negative Poisson's ratio honeycomb cell under end tensile load

A negative Poisson's ratio honeycomb cell with complex shape and in-plane loads, shown in Fig. 14, is chosen to illustrate a case where the majority of the elements undergo large displacements and small strains, posing a different behavior from the numerical examples in Section 4.1. The geometrical parameters of the cell are: length $a = 100$ mm, width $b = 100$ mm, thickness $t = 10$ mm, distance from the cell center to the inner wall $c = 20$ mm, and the width of each wall $d = 10$ mm. The isotropic material properties are: $E = 20$ GPa and $\mu = 0.3$. The left end of the cell is fixed, while a horizontal tensile load $P = 200$ kN is uniformly applied to the right end. The in-plane deformation reaches 13.5% with respect to the total length a of the honeycomb cell. The cell is divided by 304 elements with 2 elements along the thickness direction.

First, the full-order method (FOM) using hybrid-stress solid-shell formulation is compared against ABAQUS' 3D elements C3D8I, C3D8R, CSS8, and SC8R. The average stretching displacement of all nodes on the loaded end is plotted in Fig. 15, in which two different mesh densities are considered. The response curves obtained by the C3D8I and CSS8 elements are in almost perfect agreement with each other, and are not sensitive to the mesh. The solutions of SC8R and C3D8R elements converge to those of C3D8I and CSS8 elements when a fine mesh is applied. It can be seen that the solutions of ABAQUS do not match very well with that of the FOM, when the deformation is larger than 8 mm. The reason is that different element types and Lagrange formulations are applied. ABAQUS' elements and the proposed FOM adopt the updated and total Lagrange formulations, respectively. The difference caused by the two Lagrange formulations becomes obvious on nonlinear response curves when the in-plane deformation is quite large.

The accuracy of the proposed ROM is verified by comparing end stretching curves using different number of path-following steps, shown in Fig. 16. Fig. 16(b) shows the nonlinear responses obtained by the ROM using two path-following steps, almost coinciding with the exact result of the FOM. Here, each step of the ROM is equivalent to 12–18 steps of the FOM. All ABAQUS' elements used 30 path-following steps, similarly to the FOM, and required from 49 to 65 iterations. The deformed configurations and stress distribution obtained by different methods at a load of 200 kN are illustrated in Fig. 17.
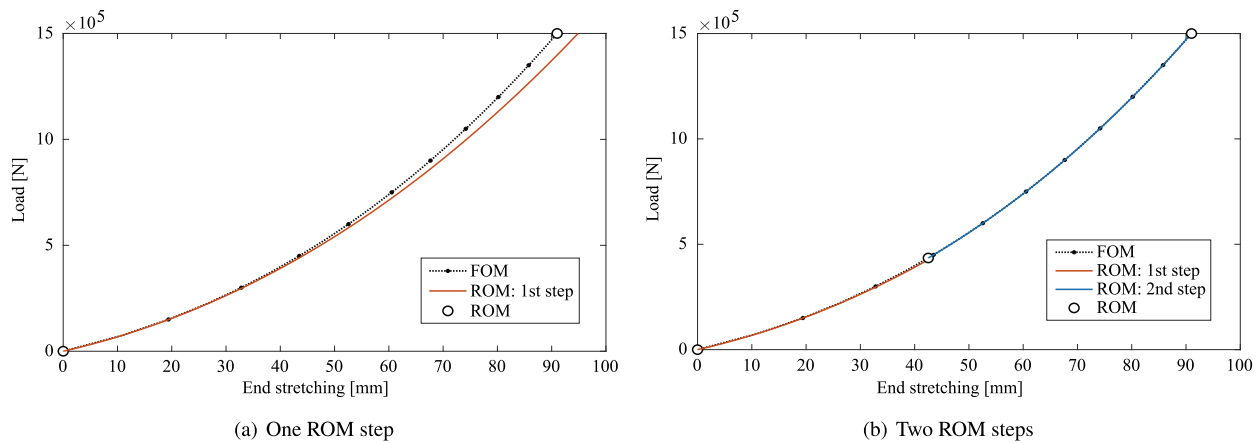
(a) One ROM step

(b) Two ROM steps

Fig. 13. Geometrically nonlinear responses of the stretched plate in horizontal direction, obtained by the reduced-order method.

Table 4
Computational time of the geometrically nonlinear analysis for the examples with three plates, using different methods.

Examples	Running time of ABAQUS [s]			Running time of in-house codes [s]	
	Minimum	Maximum	Average	FOM	ROM
Large-deflection plate	4.0 (SC8R)	5.0 (C3D8I)	4.7	4.6	1.0
Large-rotation plate	8.0 (CSS8)	13.0 (C3D8I)	10.5	15.2	5.7
Large-strain plate	5.0 (B32)	7.0 (S8R)	6.5	10.6	2.1
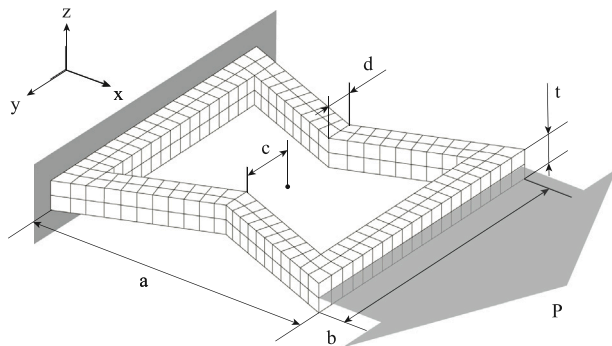
Fig. 14. The negative Poisson's ratio honeycomb cell subjected to end tensile load.

4.2.2. Swept-back box wing under end shear load

Fig. 18 shows a cantilevered swept-back box wing having five ribs and two spars, and subjected to a shear load at the tip. The geometrical parameters of the swept-back wing are: the wing span $a = 1000$ mm, chord length along the wing root $b = 500$ mm, chord length along the wing tip $c = 200$ mm, swept-back distance of the leading edge $d = 600$ mm, and intervals between two wing ribs $e = 250$ mm. The height of this wing box is $h = 50$ mm and the thickness of the skin, ribs and spars is defined to be $t = 10$ mm. The wing root is clamped, while a vertical shear load $P = 1000$ kN is uniformly applied to the wing tip. The deflection-span ratio of the plate is set to be approximately 60%. The entire wing structure is represented by 595 hexahedral elements, with a maximum span-thickness ratio of 5:1.

The proposed FOM is compared against four different elements from ABAQUS using the average displacements in the spanwise and vertical directions; measured for all the nodes at the wing tip. The corresponding response curves are plotted in Fig. 19, showing that the geometrically nonlinear responses obtained by the FOM are in agreement with the results of the CSS8 element. Results for elements SC8R and C3D8I deviate more from the solution of the FOM; however their results converge to the solution of the FOM when more finite elements are used to represent the wing structure. The response curves of the C3D8R element begin to depart from the exact solutions at

the load of 100 kN, becoming inaccurate to predict the geometrically nonlinear response. The chordwise displacement has agreed to the same extend as the spanwise and vertical displacements.

Then, the proposed ROM is compared against the FOM in Fig. 20, matching very well for all the spanwise and vertical displacements. The FOM adopts 30 path-following steps to obtain the geometrically nonlinear responses up to the load of 1000 kN, whereas the ROM requires only 4 steps. ABAQUS' elements also required from 30 to 34 path-following steps. The deformed configurations of the swept-back box wing are illustrated in Fig. 21, together with the stress distribution. The internal components are exposed in Fig. 22 for clearer observation.

5. Experimental validation using a variable-thickness plate with mixed composite-metallic materials

A cantilevered variable-thickness plate with mixed composite-metallic materials is chosen for the experimental validation. The deflection-span ratio of the plate is designed to be roughly 30%. As shown schematically in Fig. 23, the tested plate has a length of 1000 mm, width of 250 mm, and a thickness that decreases at an interval of 250 mm along the x-direction from the plate root to tip. There is a fixing device on the left end of the plate, that is, a titanium alloy fixture with a length of 180 mm and thickness of 10 mm. Three translations of all the nodes within 70 mm from the left end of the plate are restrained by the fixture. The loading device is located at 100 mm from the right end of the rectangular plate, consisting of a titanium alloy joint with a height of 175 mm. The specific geometrical parameters of the loading joint are also illustrated in Fig. 23. A vertical shear load of $P = 3136$ N is applied first to the joint bottom and then uniformly distributed to the lower surface of the plate. The whole tested structure, including the constraint fixture and loading joint, is represented by 898 hexahedral elements with a maximum span-thickness ratio of 50:1. The photographs of the test device and the deformed plate are provided in Fig. 24.

The distribution of mixed composite-metallic materials employed in the plate is illustrated in Fig. 25. The fixture and joint used for providing boundary constraints and imposing the shear load (P) are both made of a Titanium alloy Ti6Al4V (Ti). The upper part of the
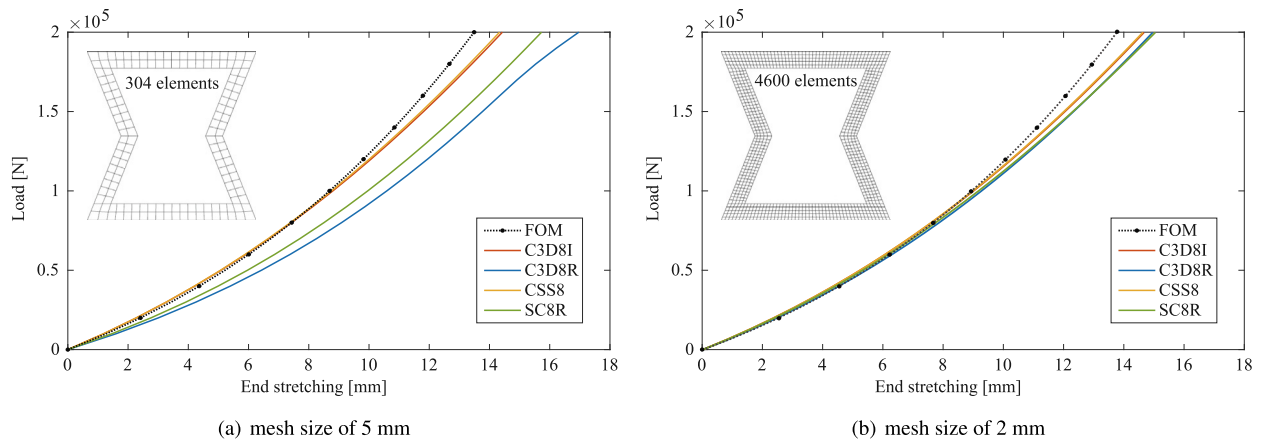
(a) mesh size of 5 mm

(b) mesh size of 2 mm

Fig. 15. Geometrically nonlinear responses of the stretched honeycomb cell, obtained by different full-order finite element methods.
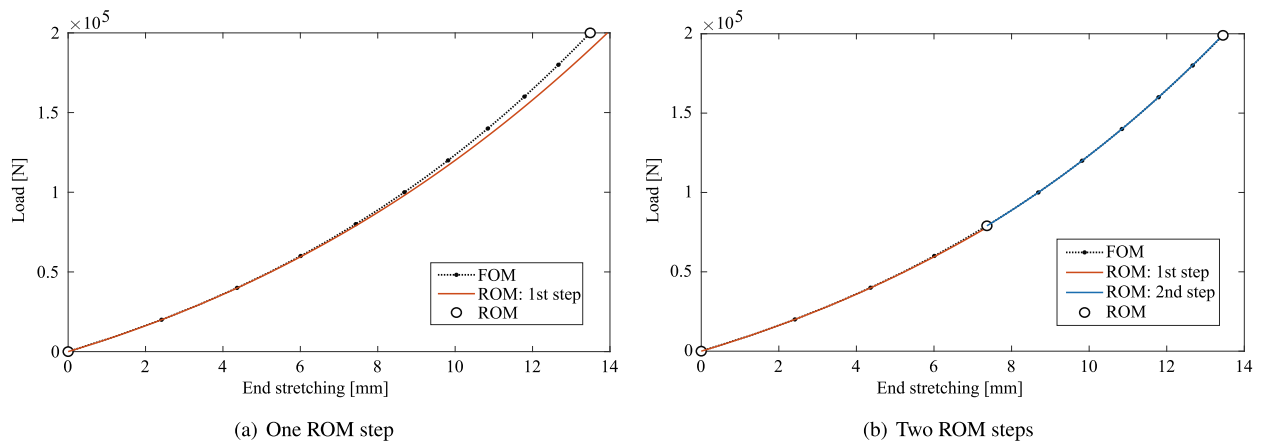

(a) One ROM step

(b) Two ROM steps

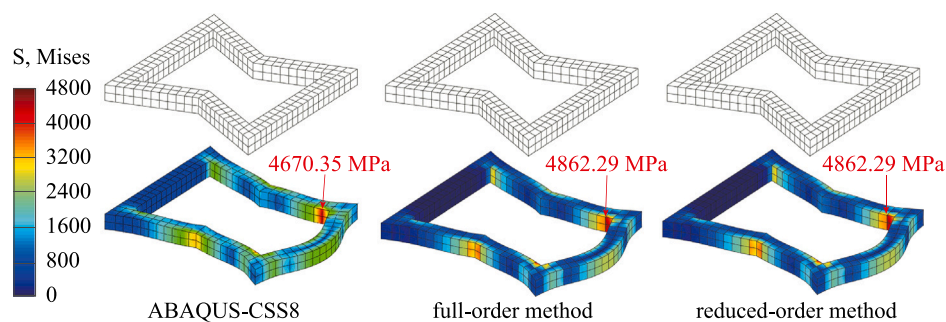**Fig. 16.** Geometrically nonlinear responses of the stretched honeycomb cell, obtained by the reduced-order method.

Fig. 17. The von Mises stress of the stretched honeycomb cell.

plate is made of an Aluminium alloy 7075 (Al), with a thickness of 15.16 mm at the left end and 1.5 mm at the right end, varying at an interval of 250 mm along the length direction. The lower part of the plate is made of composite laminates built of uni-directional carbon-epoxy material (T700), with the thickness of each layer being 0.16 mm. For the segment between the clamped region until 500 mm along the length, 24 layers with a symmetrical stacking sequence of $[0_3, 45, 0, -45, 0_2, 45, 0, -45, 0]_s$ are applied, resulting in a total thickness of 3.84 mm. The segment between 500 mm and 1000 mm along the plate length contains 16 layers, with a symmetrical stacking sequence of

$[0, -45, 0_2, 45, 0, -45, 0]_s$ and a total thickness of 2.56 mm. The specific parameters of different materials are listed in Table 5.

As shown in Fig. 26, eight points located along the symmetry line of the upper surface are identified and used to measure the deformation, which can comprehensively represent the geometrically nonlinear response of the plate. The exact distance of each measuring point to the left end of the plate is listed in Table 6.

Fig. 27 shows the comparison between the numerical results and the experimental measurements, which are represented by the triangle symbols (▲). The vertical displacement response becomes progressively
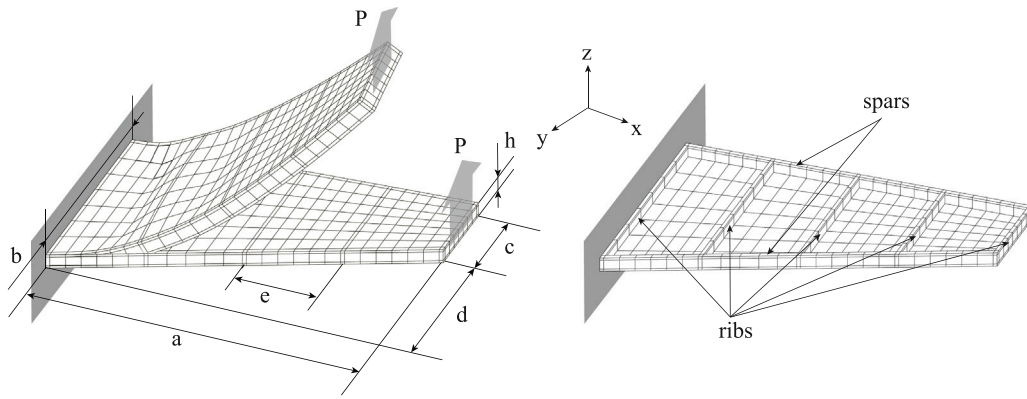
Fig. 18. The cantilevered swept-back box wing subjected to end shear load.

(a) Spanwise displacement

(b) Vertical displacement/deflection
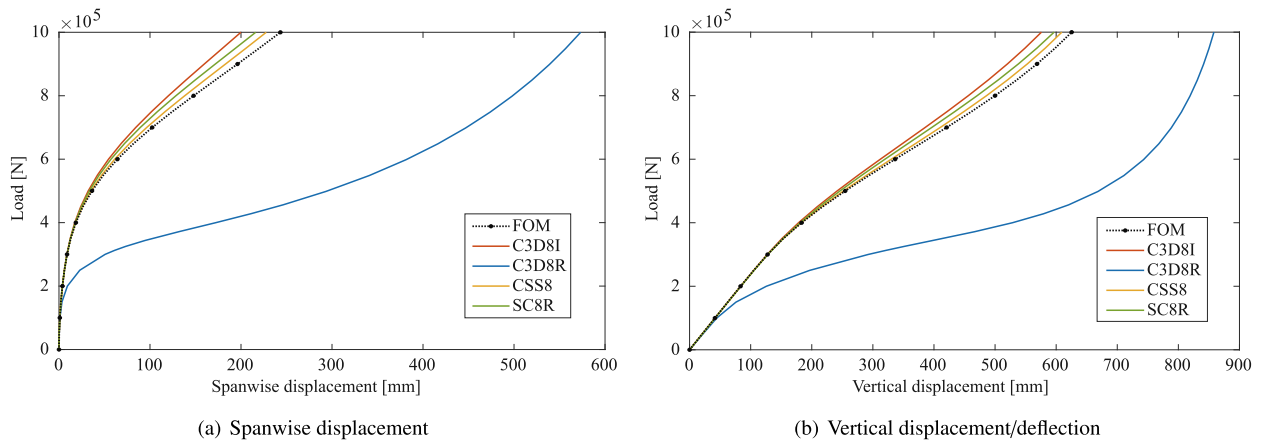
Fig. 19. Geometrically nonlinear responses of the swept-back box wing, obtained by different full-order finite element methods.

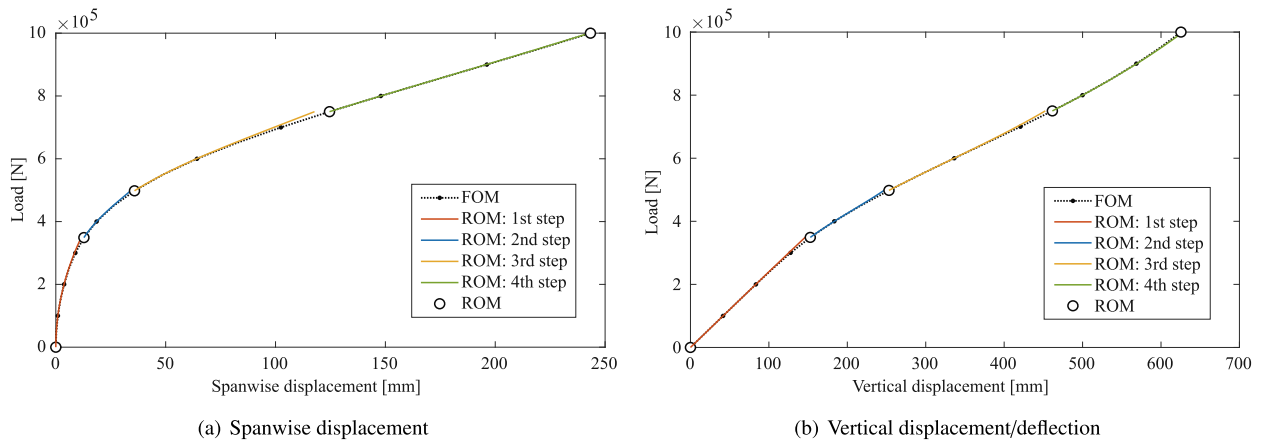(a) Spanwise displacement

(b) Vertical displacement/deflection

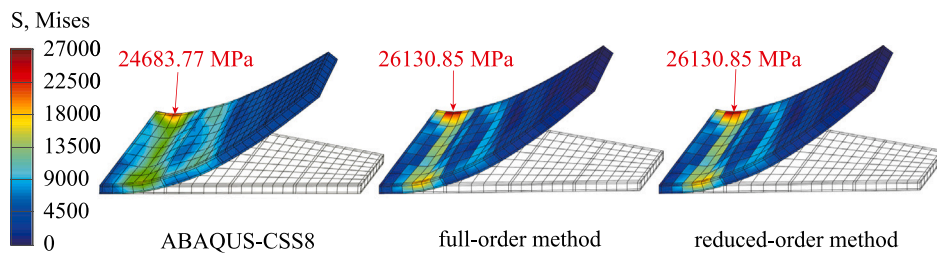**Fig. 20.** Geometrically nonlinear responses of the swept-back box wing, obtained by the reduced-order method.

Fig. 21. The von Mises stress of the swept-back box wing.
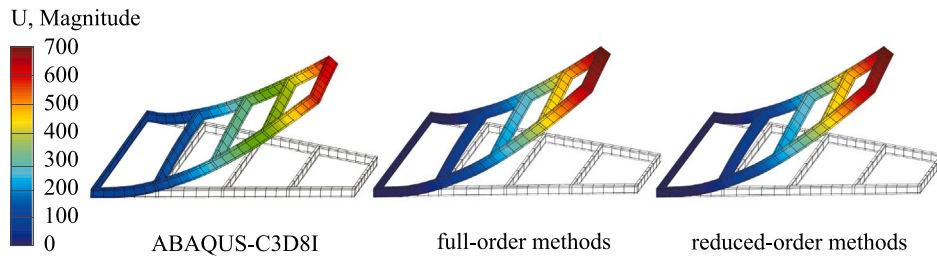
Fig. 22. Deformed configurations of the swept-back box wing without the wing upper and lower surfaces.
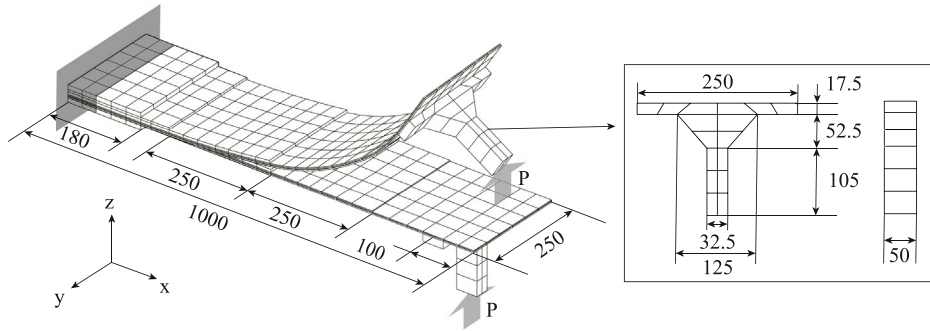
Fig. 23. The cantilevered variable-thickness plate under end shear load.
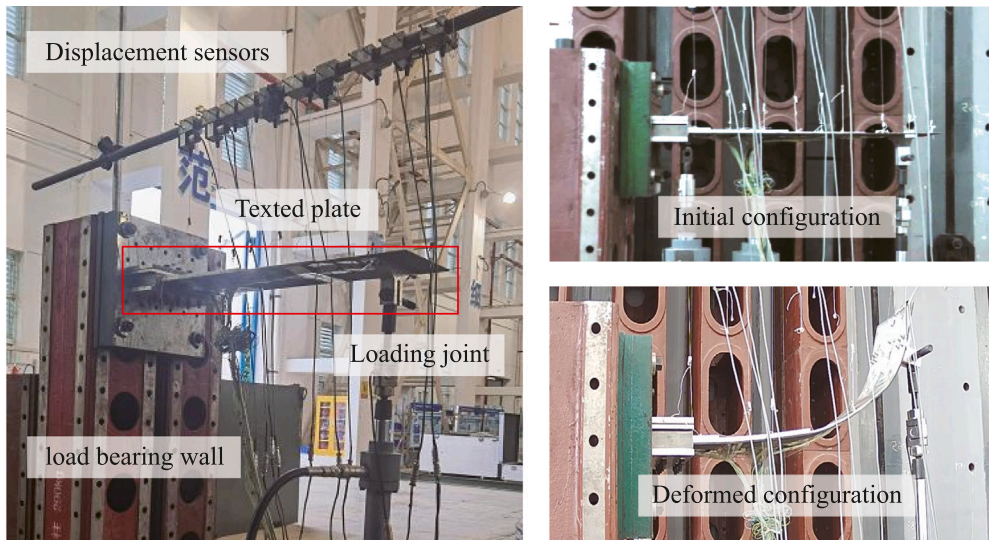
Fig. 24. The test device and deformation of the plate during the experimental test.
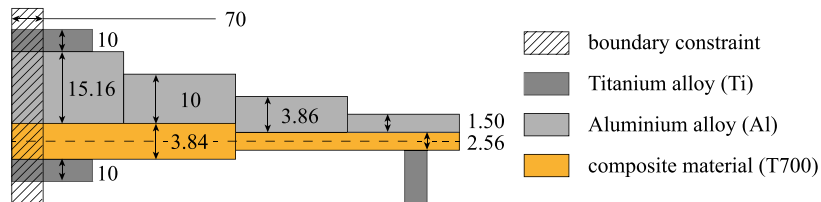
Fig. 25. Distribution of composite/alloy mixed materials and plate thickness, for the whole tested structure.

Table 5
Specific property parameters of different materials used for the plate.

Properties	Elastic modulus/MPa			Shear modulus/MPa			Poisson's ratio		
Titanium alloy (Ti)	110 000			41 353.38			0.33		
Aluminium alloy (Al)	71 000			26 691.73			0.33		
Composite material (T700)	114 000	8610	8610	4160	4160	3000	0.3	0.3	0.45
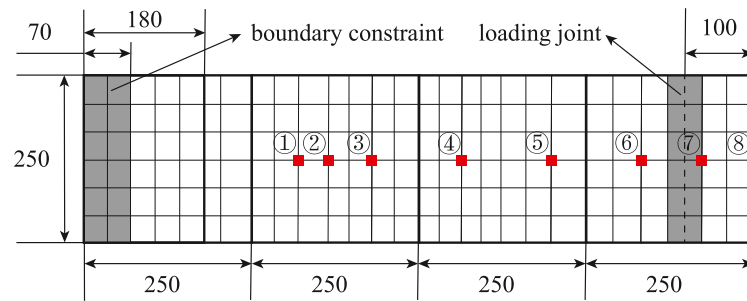
Fig. 26. Distribution of the eight displacement measuring points.

Table 6
Exact positions of the eight displacement measuring points during the experimental test.

Measuring points	1#	2#	3#	4#	5#	6#	7#	8#
Distance from constrained end/mm	205	320	430	565	625	700	835	1000

more geometrically nonlinear as the measured point moves from the root to the tip of the plate. As shown in Fig. 27, the proposed ROM requires only 3 path-following steps to trace the response curves of all the eight measurement points, accurately matching the FOM results. The deformed configurations obtained by different methods are illustrated in Fig. 28.

When comparing to the experimental test, it can be found that the numerical methods can trace the geometrically nonlinear response satisfactorily up to a load of 2400 N, when considering all the 8 measured points. However, the response curves obtained numerically begin deviating from the test results with further load increase. The differences between the numerical and experimental results are attributed to the following reasons: plastic deformation and material fracture are not considered in any of the numerical simulations, but the authors observed the irreversible deformation, that is an 8 mm deflection at the tip of the plate, after unloading, as shown in Fig. 29; insufficient details in the models regarding fixtures, load actuator and joint, leading to differences with respect to the practical test; and the stress concentrations around the screw connections that are ignored in the numerical analyses.

6. Conclusions

A geometrically nonlinear reduced-order method is developed using a hybrid-stress solid-shell formulation for three-dimensional large deformation analysis of thin-walled structures. First, an eight-node solid-shell element is established based on the Green–Lagrange kinematics, where numerical locking problems are eliminated by using the assumed natural strain method and the modified constitutive model. By using the Hellinger–Reissner total potential energy functional and the two-field variational principle, it is shown that the hybrid-stress formulation avoids the fourth-order strain energy variation with respect to the degrees of freedom, while not sacrificing the range of validity of the reduced-order model. Second, the reduced-order model with one degree of freedom is constructed much more efficiently in the hybrid-stress formulation, when compared against the established using displacement-based formulations. A novel predictor–corrector strategy is applied to trace the geometrically nonlinear response in a step-wise manner. Third, three numerical examples are used for verification, and one experimental test used to validate the computational accuracy and efficiency of the proposed reduced-order method with hybrid-stress solid-shell formulations.

Finally, a few remarks are summarized as follows: (1) The results obtained by the full-order method (FOM) using hybrid-stress solid-shell

formulations of our in-house codes are carefully compared with those calculated by ABAQUS with different commonly used elements. (2) *The accuracy of the proposed method is validated.* The response curves and deformed configurations obtained by the ROM using hybrid-stress solid-shell formulations are in perfect agreement with the results of the FOM. (3) *The applicability of the proposed method is tested.* Various structures with simple or complicated geometries are considered. Three types of geometrically nonlinear problems, that is the large deflection, large rotation, and large strain, are all involved. (3) *The efficiency of the proposed method is significant.* In terms of the computational time, the ROM is 4.7, 1.8, and 3.0 times faster than ABAQUS for the three rectangular plates subjected to various loads. The ROM requires significantly less path-following steps and iterations to trace the geometrically nonlinear response, when compared to the full-order finite element methods.

In this work, we would like to introduce an alternative tool which has great potential in geometrically nonlinear analysis, although it still has some limitations compared with the conventional methods. The main identified limitation of the proposed method is that material nonlinearities coming from plasticity or fracture are not considered in the reduced-order analysis.

CRediT authorship contribution statement

Ke Liang: Writing – original draft, Validation, Supervision, Software, Resources, Project administration, Methodology, Investigation, Funding acquisition, Formal analysis, Conceptualization. **Jiaqi Mu:** Visualization, Investigation, Formal analysis. **Saullo G.P. Castro:** Writing – review & editing, Supervision, Methodology.
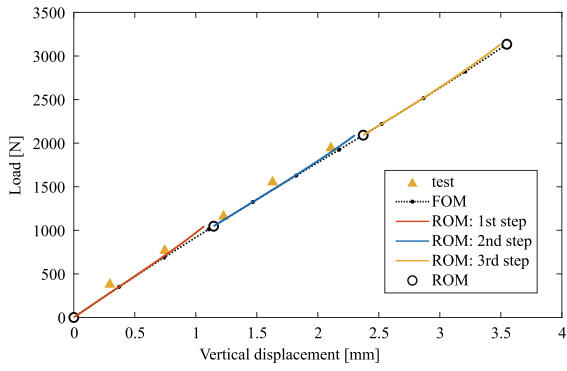
Declaration of competing interest

The authors declare that they have no known competing financial interests or personal relationships that could have appeared to influence the work reported in this paper.
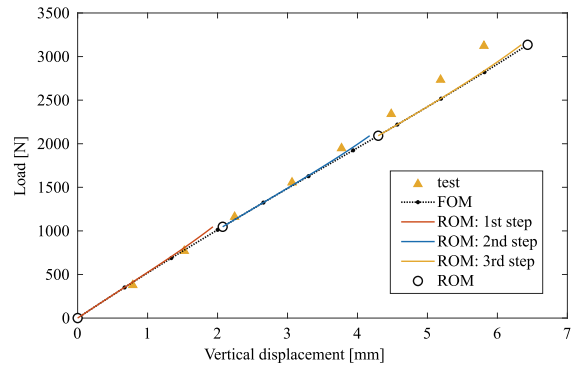
Acknowledgments

Data availability

Data will be made available on request.
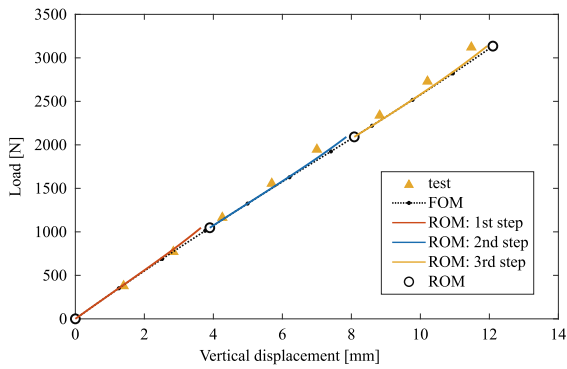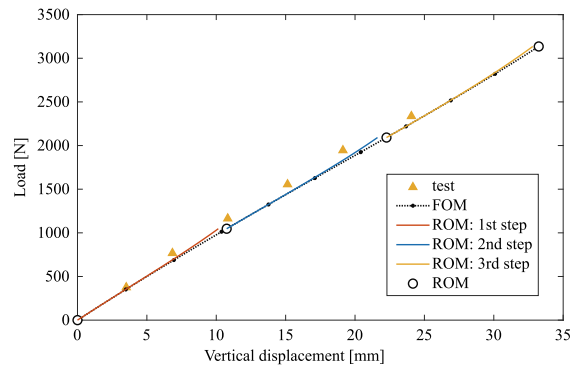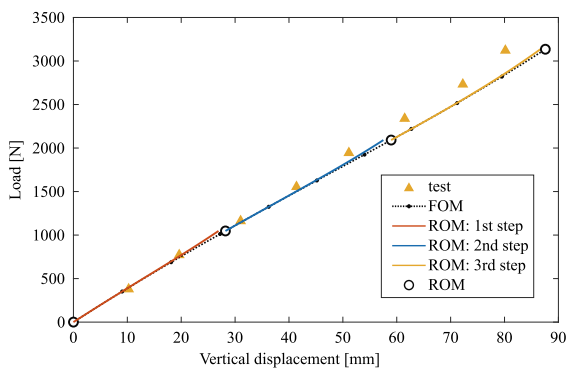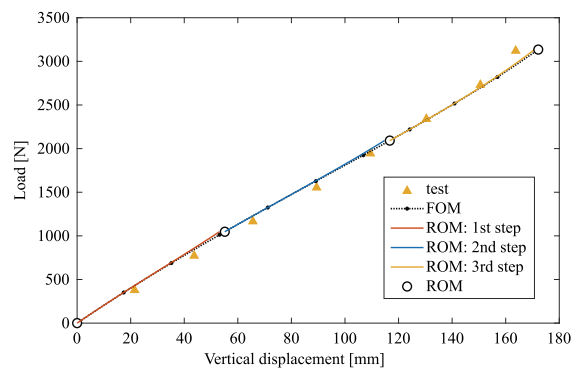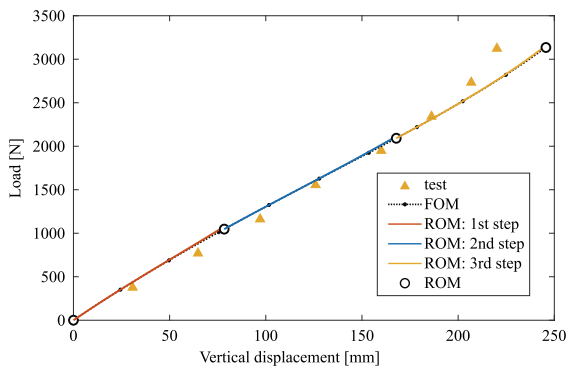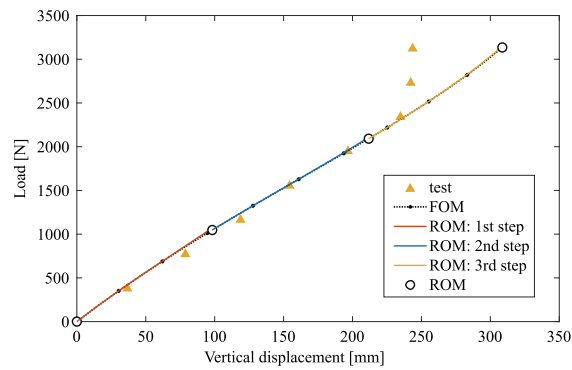
Fig. 27. Geometrically nonlinear responses of the variable-thickness plate, obtained by the reduced-order method.
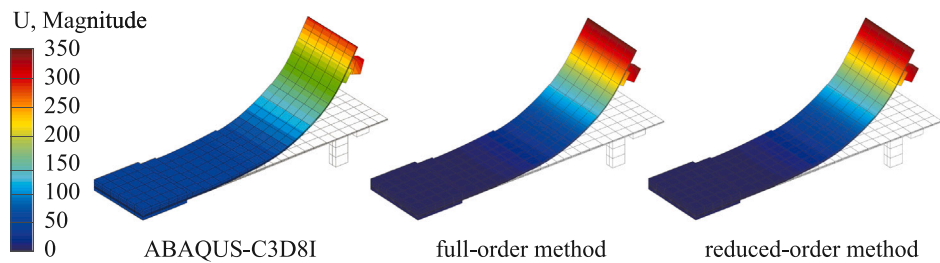
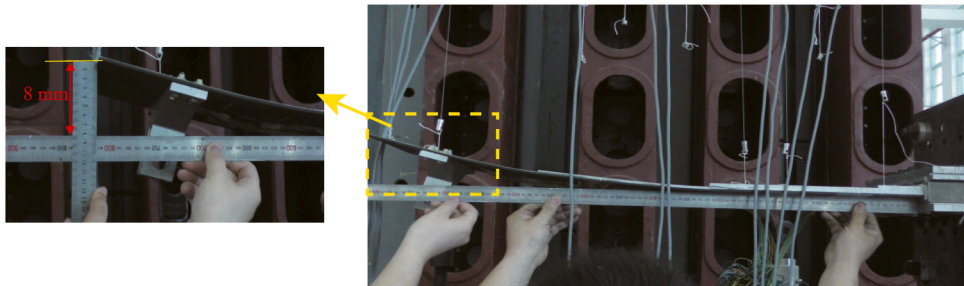**Fig. 28.** Deformed configurations of the variable-thickness plate.

Fig. 29. The irreversible deformation (8 mm deflection) of the plate after unloading.

References

Barbero, E., Madeo, A., Zagari, G., Zinno, R., Zucco, G., 2014. Koiter asymptotic analysis of folded laminated composite plates. Compos. Part B: Eng. 61, 267–274.

Castro, S.G.P., 2015. Semi-Analytical Tools for the Analysis of Laminated Composite Cylindrical and Conical Imperfect Shells Under Various Loading and Boundary Conditions (Ph.D. thesis). Clausthal University of Technology, http://dx.doi.org/10.21268/20150210-154320.

Castro, S.G.P., Jansen, E.L., 2021. Displacement-based formulation of Koiter's method: application to multi-modal post-buckling finite element analysis of plates. Thin-Walled Struct. 159, 107217.

Castro, S.G.P., Jansen, E.L., 2022. Displacement-based multi-modal formulation of Koiter's method applied to cylindrical shells. In: AIAA SCITECH 2022 Forum. p. 0256.

Cea, A., Palacios, R., 2020. A non-intrusive geometrically nonlinear augmentation to generic linear aeroelastic models. J. Fluids Struct. 101, 103222.

Cea, A., Palacios, R., 2022. Geometrically nonlinear effects on the aeroelastic response of a transport aircraft configuration. J. Aircr. 60 (1), 1–16.

Drachinsky, A., Raveh, D.E., 2020. Modal rotations: a modal-based method for large structural deformations of slender bodies. AIAA J. 58 (7), 3159–3173.

Garcea, G., 2001. Mixed formulation in Koiter analysis of thin-walled beams. Comput. Struct. 190, 3369–3399.

Garcea, G., Madeo, A., Zagari, G., Casciaro, R., 2009. Asymptotic postbuckling fem analysis using corotational formulation. Int. J. Solids Struct. 46, 377–397.

Garcea, G., Salerno, G., Casciaro, R., 1999. Extrapolation locking and its sanitization in Koiter's asymptotic analysis. Comput. Methods Appl. Mech. Engrg. 180, 137–167.

Henrichsen, S.R., Weaver, P.M., Lindgaard, E., Lund, E., 2016. Post-buckling optimization of composite structures using Koiter's method. Internat. J. Numer. Methods Engrg. 108, 902–940.

Kazinakis, K., Kyriakides, S., Jiang, D., Bechle, N.J., Landis, C.M., 2021. Buckling and collapse of pseudoelastic NiTi tubes under bending. Int. J. Solids Struct. 221, 2–17.

Koiter, W.T., 1967. On the Stability of Elastic Equilibrium. National Aeronautics and Space Administration.

Lanzo, A.D., Garcea, G., Casciaro, R., 1995. Asymptotic post-buckling analysis of rectangular plates by HC finite elements. Internat. J. Numer. Methods Engrg. 38, 2325–2345.

Liang, K., Abdalla, M., Gürdal, Z., 2013. A Koiter-Newton approach for nonlinear structural analysis. Internat. J. Numer. Methods Engrg. 96, 763–786.

Liang, K., Ruess, M., Abdalla, M., 2014. The Koiter-Newton approach using *von Kármán* kinematics for buckling analyses of imperfection sensitive structures. Comput. Methods Appl. Mech. Engrg. 279 (1), 440–468.

Liguori, F.S., Madeo, A., 2021. A corotational mixed flat shell finite element for the efficient geometrically nonlinear analysis of laminated composite structures. Internat. J. Numer. Methods Engrg. 122, 4575–4608.

Magisano, D., Leonetti, L., Garcea, G., 2017. Advantages of the mixed format in geometrically nonlinear analysis of beams and shells using solid finite elements. Internat. J. Numer. Methods Engrg. 109, 1237–1262.

Magisano, D., Liang, K., Garcea, G., Leonetti, L., Ruess, M., 2018. An efficient mixed variational reduced-order model formulation for nonlinear analyses of elastic shells. Internat. J. Numer. Methods Engrg. 113, 634–655.

Pian, T.H., 1985. Finite elements based on consistently assumed stresses and displacements. Finite Elem. Anal. Des. 1, 131–140.

Rong, Y., Sun, Q., Liang, K., 2022. Modified unified co-rotational framework with beam, shell and brick elements for geometrically nonlinear analysis. Acta Mech. Sin. 38, 421136.

Salerno, G., Lanzo, A.D., 1997. A nonlinear beam finite element for the post-buckling analysis of plane frames by Koiter's perturbation approach. Comput. Methods Appl. Mech. Engrg. 146, 325–349.

Sze, K., Chan, W., Pian, T., 2002. An eight-node hybrid-stress solid-shell element for geometric non-linear analysis of elastic shells. Internat. J. Numer. Methods Engrg. 55, 853–878.

Sze, K.Y., Liu, X.H., Lo, S.H., 2004. Popular benchmark problems for geometric nonlinear analysis of shells. Finite Elem. Anal. Des. 40 (11), 1551–1569.

Tiso, P., 2006. Finite Element Based Reduction Methods for Static and Dynamic Analysis of Thin-Walled Structures (Ph.D. thesis). Delft University of Technology.

Wang, X.Q., Perez, R.A., Mignolet, M.P., 2013. Nonlinear reduced order modeling of complex wing Models. In: 54th AIAA/ASME/ASCE/ AHS/ASC Structures, Structural Dynamics, and Materials Conference. pp. AIAA Paper 2013–1520.

Zagari, G., 2009. Koiter's Asymptotic Numerical Methods for Shell Structures Using a Corotational Formulation (Ph.D. thesis). Universita Della Calabria.

Zhang, W., Kyriakides, S., 2024. Winding and unwinding a pipe with Lüders bands on a reel. Part I: Analysis of base case. Int. J. Solids Struct. 290, 112687.